energies

MDPI

*Article*

# Numerical Analysis of Space Charge Behavior and Transient Electric Field under Polarity Reversal of HVDC Extruded Cable

**Sun-Jin Kim and Bang-Wook Lee ***

Department of Electrical and Electronic Engineering, Hanyang University, Ansan 15588, Korea; ksj8119@hanyang.ac.kr

* Correspondence: bangwook@hanyang.ac.kr

Received: 9 April 2020; Accepted: 28 May 2020; Published: 3 June 2020




**Abstract:** The superimposed transient electric field generated by polarity reversal causes severe stress to the high-voltage direct current (HVDC) cable insulation. Especially for polymeric insulation materials, space charge accumulation is prominent, which strengthens local electric field intensity. In order to avoid the risk of dielectric breakdown resulting from an intensified electric field caused by space charge behavior, several numerical analyses have been conducted using the Bipolar Charge Transport (BCT) model. However, these studies have only considered a unidirectional electric field assuming only steady state operating conditions, and there are few works that have analyzed space charge behavior during transient states, especially for the polarity reversal period. In order to analyze the charge behavior under polarity reversal, it is necessary to establish the boundary condition considering the direction and intensity of the field. Therefore, in this paper, we proposed a modified model connecting the steady state to the polarity reversal state, and the transient electric field was investigated depending on the electric potential zero duration. Since space charge behavior is influenced by temperature, different load currents were considered. From the simulation results, it was observed that the capacitive field was dominant on the electric field distribution during the polarity reversal. In addition, the long electric potential zero duration and high load currents could contribute to form a homo-charge at the conductor within the time of polarity reversal, resulting in a noticeable decrease in the maximum electric field intensity.

**Keywords:** bipolar charge transport model; voltage polarity reversal; space charge behavior; cable insulation; dielectrics

## 1. Introduction

High-voltage direct current (HVDC) transmission has many advantages compared to high-voltage alternating current (HVAC) transmission in terms of transmission distance, power losses, and connecting nonsynchronous networks [1,2]. Oil-filled (OF) cable and mass-impregnated (MI) cable have been used in the past as a transmission medium, but recently, there has been an increasing tendency to use the extruded polymer cable because of its advantages in terms of electrical and mechanical properties, conductor temperature, cost, and system length [3,4]. However, due to the chemical structure of polymeric insulation, space charge accumulates in insulation materials under DC stress that can lead to electric field distortion.

There are generally two numerical models for the study of dielectrics properties in DC systems. One is a macroscopic model based on the conductivity of an insulation composed of temperature and electric field dependence coefficients. The other is a Bipolar Charge Transport (BCT) model that can microscopically analyze space charges by describing the dynamics of charges within the insulation [5,6].

Recently, the BCT model started from the parallel specimen structure has been improved to be applied to cylindrical configuration [7,8]. Because the cylindrical structure has temperature gradients and there is variation in the electric field along the radius, a more advanced and complex model should be applied compared to the parallel geometry.

Most studies have only considered positive voltage application conditions that generate a unidirectional electric field in dielectrics, whereas no model has been reported considering polarity reversal [9,10]. In practice, the operating states of HVDC cable are divided into several stages depending on the operating conditions of the power system. Each stage consists of the transient state, switching on/off and polarity reversal where voltage fluctuations occur, and the steady state [11]. The polarity reversal stage becomes a problem in the line commutated converter (LCC) system that can change the power flow by reversing the polarity of the voltage while maintaining the direction of the current flow. Under the polarity reversal of the LCC system, transient field distortion occurs, which causes severe stress on the cable. In particular, when there is a temperature gradient across the insulation, it is known that a high electric field occurs at the conductor immediately after the polarity of the applied voltage is reversed [12]. Therefore, it is necessary to analyze the space charge behavior and electric field according to temperature under polarity reversal conditions.

In this work, we focused on numerical analysis of a low-density polyethylene (LDPE) cable geometry using the BCT model to investigate the transient electric field considering space charge dynamics under several polarity reversal conditions. Unlike the existing model considering only unidirectional DC applied voltage, we proposed the modified boundary condition to cover the charge behavior at each interface between the dielectric and electrodes because the anode and cathode are reversed within a short time. In addition, since the actual cable temperature gradient is generated by the Joule heat of the load current flowing through the conductor and the temperature is a major factor in the behavior of the charge, the space charge behavior and the transient electric field were analyzed by varying the load current.

## 2. Description of Bipolar Charge Transport Model

### *2.1. Overall Bipolar Charge Transport Model*

The BCT model is designed to describe the transport of electrons and holes in polymeric insulation materials and to estimate the mechanism of space charge accumulation. This model is driven by five charge transport processes: Injection, hopping, trapping, de-trapping, and recombination, as shown in Figure 1 [13].

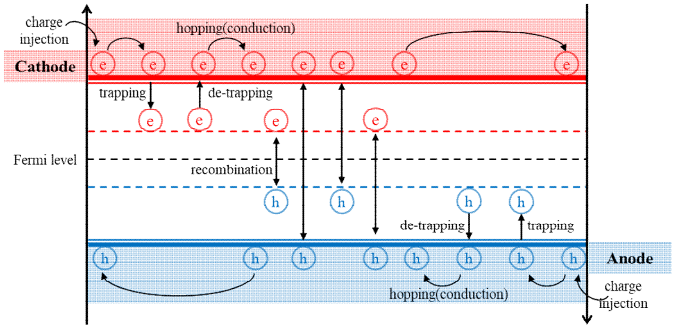



**Figure 1.** Overall mechanism of the Bipolar Charge Transport (BCT) model.

First, when the electric field at the interface between the electrode and the insulation exceeds the threshold field, a large amount of carrier is injected and mobile charges in the insulation are generated. Each injected mobile charge moves to the opposite electrode along the direction of the applied electric field. These charges hop shallow traps in the energy band gap, and this process is called hopping or conduction. In addition, charges can be trapped in deep traps caused by chemical defects during

hopping. This phenomenon is called trapping, while the escape of charges from deep traps is called de-trapping. When de-trapping, trapped charges become mobile charges again and participate in the hopping process. Finally, when recombination of charges occurs, they are neutralized and no longer have polarity, so they do not affect the space charge distribution.

### 2.2. Governing Equations

To describe the processes of charge dynamics in the cylindrical insulation, the following governing equations are used: The transport Equation (1), current continuity Equation (2), and Poisson's Equation (3).

$$j_c(r,t) = \mu_c(r,t) n_{cm}(r,t) E(r,t) \tag{1}$$

$$\frac{\partial n_{cm,ctr}(r,t)}{\partial t} + \frac{1}{r}\frac{\partial j_c(r,t)}{\partial r} = s_{cm,ctr}(r,t) \tag{2}$$

$$\frac{\partial^2 V(r,t)}{\partial r^2} + \frac{1}{r}\frac{\partial V(r,t)}{\partial r} = -\frac{\rho(r,t)}{\varepsilon_0 \varepsilon_r} \tag{3}$$

where $j_c$ is the transport current density related to hopping type mobility $\mu$, the charge density is $n_c$, and the applied electric field is $E$. The subscript $c$ refers to the electron or hole, and $m$ or $tr$ refers to the mobile or trapped charge, respectively. The net charge density is $\rho$, $\varepsilon_0$ is the vacuum permittivity ($\varepsilon_0 = 8.854 \times 10^{-12}$ (F/m)), and $\varepsilon_r$ is the relative dielectric permittivity ($\varepsilon_r = 2.3$). The source term is $s_{cm,ctr}$, which denotes the changes in the local density due to processes other than transport (trapping, de-trapping, or recombination).

Since the radial temperature and electric field distribution are different in the cylindrical configuration, the following hopping type mobility Equation (4) was used [8]:

$$\mu_{e,h}(r,t) = \frac{2dv}{E(r,t)} \exp\left(\frac{e w_{\mu e,\mu h}}{k_B T(r)}\right) \sinh\left(\frac{eE(r,t)d}{2k_B T(r)}\right) \tag{4}$$

where $d$ is the distance between traps ($d = 3.8 \times 10^{-9}$ (m)), $v = k_B T/h$ is the attempt to escape the frequency, $k_B$ is Boltzmann's constant ($k_B = 1.38 \times 10^{-23}$ (J/K)), $h$ refers to a Planck's constant ($h = 6.62 \times 10^{-34}$ (J/s)), and $e$ is elementary charge ($e = 1.6 \times 10^{-19}$ (C)).

The extent of the trapping process ($T_c$) is described by the trapping coefficient $B_{e,h}$, which reflects the probability of capturing the charges per unit of time. In addition, the de-trapping coefficient ($D_c$) expresses the probability of escaping from traps by overcoming the potential barrier height $w_{tre,trh}$.

$$T_c = B_c n_{cm}\left(1 - \frac{n_{ctr}}{N_{ctr}}\right) \tag{5}$$

$$D_c = v \exp\left(-\frac{e w_{ctr}}{k_B T(r)}\right) \tag{6}$$

where $N_{ctr}$ is the total density of the deep traps.

Since recombination is also influenced by the charge mobility, the recombination coefficient ($S_{c\mu}$) was written as a function of temperature and electric field strength.

$$S_{c\mu}(r,t) = \frac{\mu_e(r,t) + \mu_h(r,t)}{\varepsilon_0 \varepsilon_r} \tag{7}$$

The Schottky injection of the charge carrier occurs when the applied electric field at the interface between the electrode (conductor or sheath) and the dielectric exceeds a threshold electric field of about 10 kV/mm [14,15]. Therefore, the Schottky injection was defined to occur at both interfaces only

when the electric field was over the threshold value. The temperatures corresponding to the positions of both interfaces were applied to the T term of the equation at each time step.

$$j_{sch}(r,t) = AT(r)^2 \exp\left(\frac{-ew_{e,hi}}{k_B T(r)}\right) \exp\left(\frac{e}{k_B T(r)} \sqrt{\frac{eE(r,t)}{4\pi\varepsilon_0\varepsilon_r}}\right) \quad (8)$$

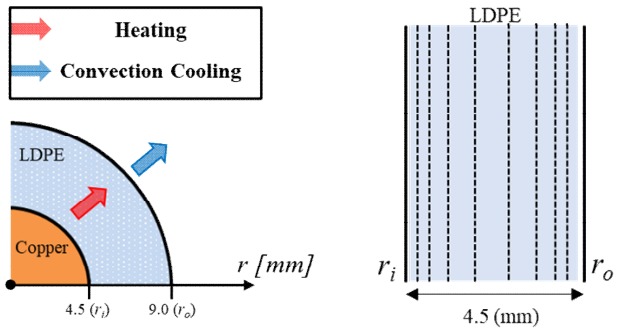
where $A$ is Richardson's constant ($A = 1.2 \times 10^6$ (A/(m$^2$·K$^2$))).

## 3. Application of Bipolar Charge Transport Model to Polarity Reversal Duration

### 3.1. Simulation Conditions

The operational stages of the HVDC cable are defined as seven stages. Each stage consists of the transient state, switching on/off and polarity reversal with voltage varying, and DC steady state. In this study, we focused on the polarity reversal where the most severe electric field occurs.

A one-dimensional cylindrical geometry with a copper conductor radius ($r_i$) of 4.5 mm and an outer radius ($r_o$) of 9 mm was used for the simulations, as shown Figure 2a. Figure 2b shows the mesh grid set smaller as it is closer to both interfaces. The parameters used for the simulations are given Table 1 [6–9,16].




(**a**) (**b**)

**Figure 2.** Schematic representation of the cable geometry (**a**), and the one-dimensional grid used for the simulation (**b**).

**Table 1.** Parameters used for the simulations.

| Parameter | Value | Units |
|---|---|---|
| Injection barrier heights | | |
| $w_{ei}$ for electrons | 1.27 | eV |
| $w_{hi}$ for holes | 1.16 | eV |
| Trapping coefficients | | |
| $B_e$ for electrons | 0.1 | 1/s |
| $B_h$ for holes | 0.2 | 1/s |
| Trap depths (for hopping) | | |
| $w\mu_e$ for electrons | 0.71 | eV |
| $w\mu_h$ for holes | 0.65 | eV |
| Trap densities | | |
| $n_{oet}$ for electrons | 100 | C/m$^3$ |
| $n_{oht}$ for holes | 100 | C/m$^3$ |
| De-trapping barrier heights | | |
| $w_{tre}$ for electrons | 0.96 | eV |
| $w_{trh}$ for electrons | 0.99 | eV |

First, a positive voltage of 90 kV was applied at conductor for 10,000 s, and then two types of polarity reversal waveforms were applied, as shown Figure 3. One was applied when the voltage switched linearly to negative polarity for 120 s. The other was applied after the voltage was switched off. The electric potential zero was maintained for a certain time (60 s, 1800 s), and then the voltage was switched to negative polarity.

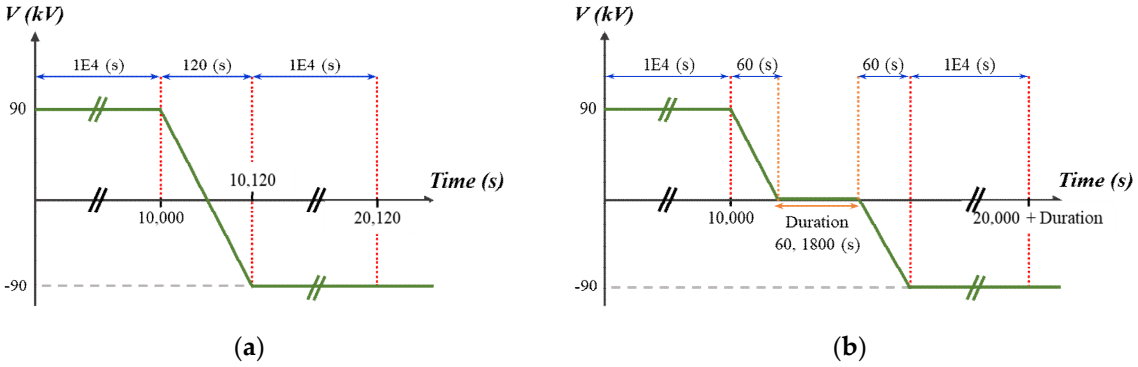



**Figure 3.** Applied polarity reversal voltage waveforms: (**a**) Without electric potential zero duration; (**b**) with electric potential zero duration.

In the case of the cable structure, the temperature gradient within the insulation occurs depending on the load current, which causes the field distribution and the location of the maximum field intensity to change. Moreover, the governing equations of the BCT model also depend on temperature. Therefore, for a more realistic situation, different load currents were set to simulate the temperature distribution within the dielectrics.

In this work, the temperature distribution inside the insulation was simulated by the heat transfer Equation (9). Currents of 250 A and 350 A were applied to the conductors and the characteristics of the space charge behavior were analyzed under different temperature conditions.

$$\rho_d C_p \frac{\partial T}{\partial t} = \nabla \cdot (k \nabla T) + Q \tag{9}$$

where $\rho_d$ is the density of material ($\rho_d$ = 920 (kg/m$^3$)), $C_p$ is the heat capacity at constant pressure ($C_p$ = 1900 (J/(kg·K))), $k$ is the thermal conductivity ($k$ = 0.33 (W/(m·K))), and $Q$ is the heat source from the conductor of cable.

The amount of heat generated can be calculated following Equations (10)–(14). Heat generated from the conductor is spread through the LDPE and cooled by convective heat flux at the sheath side. The convective heat flux (Equation (10)) was set as the boundary condition at the sheath side. In addition, the resistance of the conductor has different values depending on AC and DC, as shown in Equation (11). The object of this simulation was a single-core DC cable structure, so skin effects ($y_s$) and proximity effects ($y_p$) were excluded. The resistivity and temperature coefficient are given Table 2 [17–19].

$$q_0 = h(T_{ext} - T) \tag{10}$$

$$R_{AC} = R_{DC}(1 + y_s + y_p) \tag{11}$$

$$Q = I^2 R_{DC} \tag{12}$$

$$R_{DC} = R_{20}[1 + \alpha_{20}(\theta_c - 20)] \tag{13}$$

$$R_{20} = \frac{1.02 \times 10^{12} \rho_{20}}{A_c} \tag{14}$$

where $I$ is the DC current, $R_{DC}$ is the DC conductor resistance, $R_{20}$ is the conductor resistance at 20 °C, $\alpha_{20}$ is the temperature coefficient at 20 °C for the copper, $\theta_c$ is the operating temperature, $\rho_{20}$ is the copper resistivity at 20 °C, and $A_c$ is the cross section of the conductor.

**Table 2.** Resistivity and temperature coefficient.

| Material | Resistivity (Ω·m) | Temperature Coefficient (1/K) |
|---|---|---|
| Copper | $1.7247 \times 10^{-8}$ | $3.93 \times 10^{-3}$ |
| Aluminum | $2.8264 \times 10^{-8}$ | $4.03 \times 10^{-3}$ |

Figure 4 shows the time-varying temperatures on the conductor and sheath side with the applied current. In both results, the temperature was saturated after about 3000 s. Figure 4a shows a temperature gradient of about 7 °C when the current was 250 A, and the conductor and sheath temperature were about 41 °C and 34 °C, respectively. Figure 4b shows a temperature gradient of about 13 °C when the current was 350 A, and the conductor and sheath temperature were about 64 °C and 51 °C, respectively.

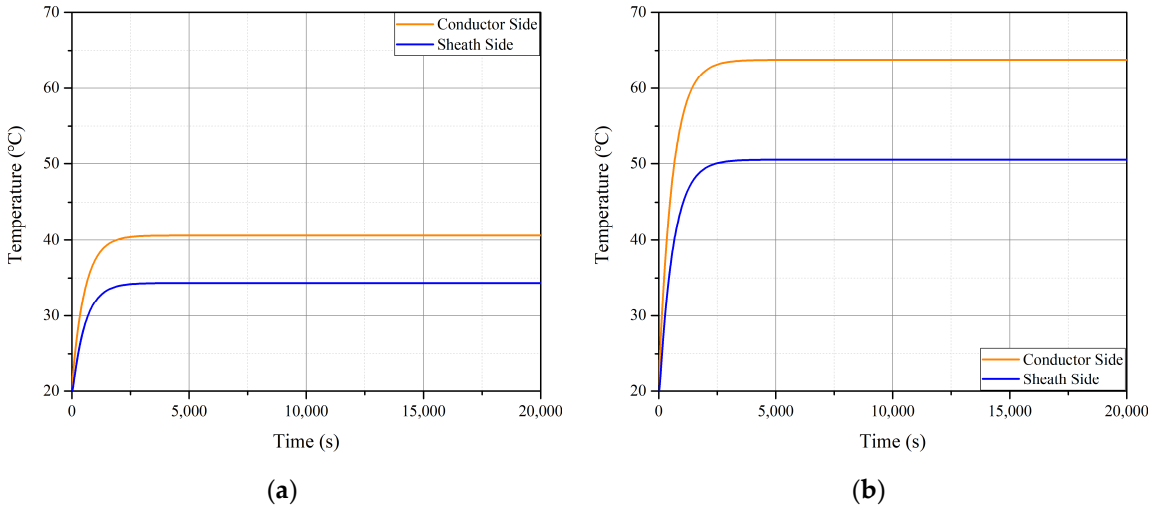



**Figure 4.** Time-varying temperature of the cable conductor and sheath according to the applied current: (**a**) 250 A; (**b**) 350 A.

### *3.2. Modification of Boundary Condition Considering Polarity Reversal*

Figure 5 shows the modified boundary condition considering polarity reversal. The Schottky injection is a mechanism in which a large amount of charge is injected when the electric field exceeding a threshold value is applied. In the case of field intensity below a threshold, a linear conduction equation was additionally applied as a boundary condition to define charge injection. This equation was defined as a first order function that connects the zero point at the Schottky current density value corresponding to the field intensity 10 kV/mm to avoid discontinuity during the numerical analysis process.

Since the anode and cathode are reversed at the time when the polarity of the applied voltage is reversed, the direction of the electric field has to be considered to simulate the transient analysis. In order to express that the injection of electrons and holes at each interface was converted to extraction, the extraction current density was set in the opposite direction of the existing electric field and defined by the transport Equation (1). This equation also includes variables of mobile charge density and mobility, so the amount of charge extraction was determined depending on the temperature, as well as the electric field.

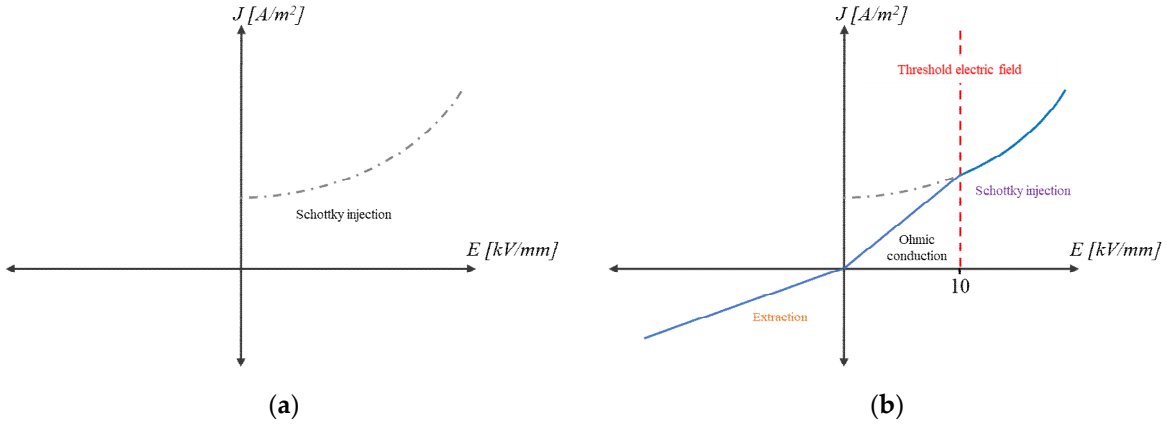



**Figure 5.** Modification of boundary conditions considering polarity reversal: (**a**) Conventional condition; (**b**) modified condition.

In the case of the existing model, the mobile holes are injected from conductor (anode) and set to flow out when mobile holes reach the opposite sheath electrode (cathode). The current density is applied to the Schottky injection equation regardless of the field strength. However, in order to analyze the transient state of the cable system, it is necessary to set the modified boundary conditions considering the threshold and direction of electric field. The boundary conditions of both interfaces for mobile holes are briefly shown in Figure 6. Boundary conditions for mobile electrons were also modified in the same way. The electric field was set to a positive value when the direction of field was outward radial. The process of charge injection and extraction at the conductor by the boundary conditions was as follows:

- Since the electric field at the conductor interface after the start of voltage application was above the threshold electric field, mobile holes were injected by the Schottky injection.
- Over time, the electric field at conductor was lowered below the threshold value by homo-charge, and the linear conduction equation was applied.
- When the direction of the electric field was reversed, the conductor became a cathode and the mobile holes were extracted.
- In addition, the reversed electric field strength was gradually intensified over time, and the mobile electrons were injected from the conductor.

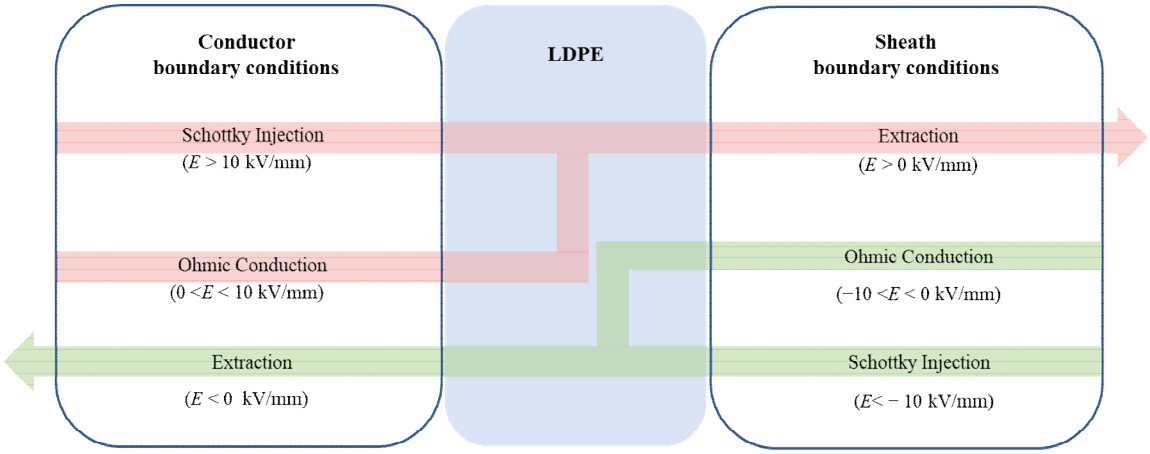



**Figure 6.** Modified boundary conditions considering both the direction and intensity of field. Red is direction of mobile holes at $E > 0$; green is direction of mobile holes at $E < 0$.

As a result, injection or extraction of charges was determined according to the direction and intensity of electric field at both interfaces. These modified boundary conditions enabled the analyses of the transient states such as the polarity reversal or superimposed impulse voltage.

## 4. Results and Discussion

### *4.1. Polarity Reversal without Electric Potential Zero Duration*

Figure 7 shows the time-varying space charge distribution on the conductor and sheath sides during the polarity reversal when the applied current was 250 A. The space charge density was truncated in the legend in order to observe the charge movement. As shown in Figure 7, there was little change in the charge distribution at both conductor and sheath. This was a result of the slow charge mobility due to the low temperature. In addition, it can be seen through the time-varying electric field distribution in Figure 8 that the change in electric field intensity was caused by a simple potential difference of the reversed voltage. Immediately after the polarity reversal, the electric field intensity at the conductor interface was derived to 57.67 kV/mm by a capacitive field Equation (15) [20]. Since this result is similar to the simulated field strength of 56.34 kV/mm as shown in Figure 8b, it means that little change occurred in space charge distribution.

$$E_{AC}(r) = \frac{U_0}{r \ln(r_o/r_i)} \tag{15}$$

The homo-charge refers to the charge, the same sign as the adjacent electrode, and reduces the local electric field strength at the interface. On the contrary, the hetero-charge is opposite to the adjacent electrode and locally increases the field intensity at the interface [21]. As a result, when the voltage application time was 10,120 s, the hetero-charge was formed and the maximum electric field strength occurred at the interface between the conductor and LDPE.

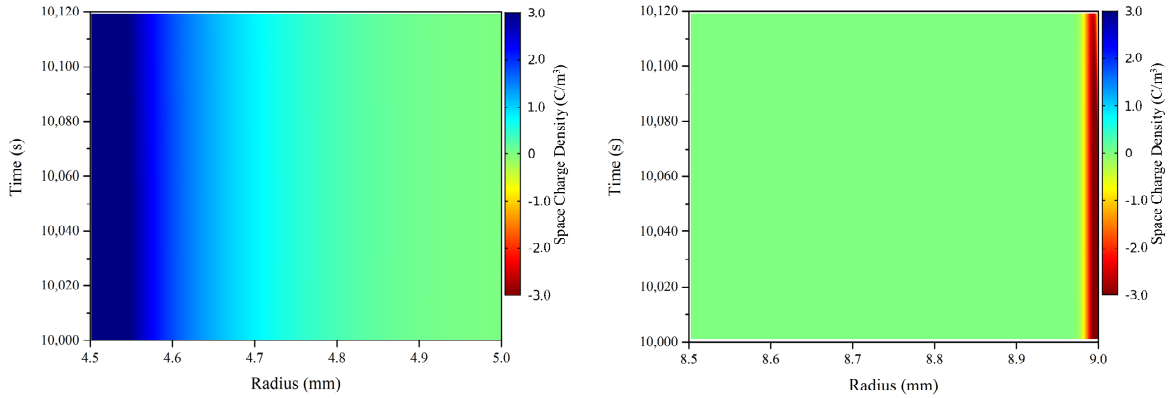
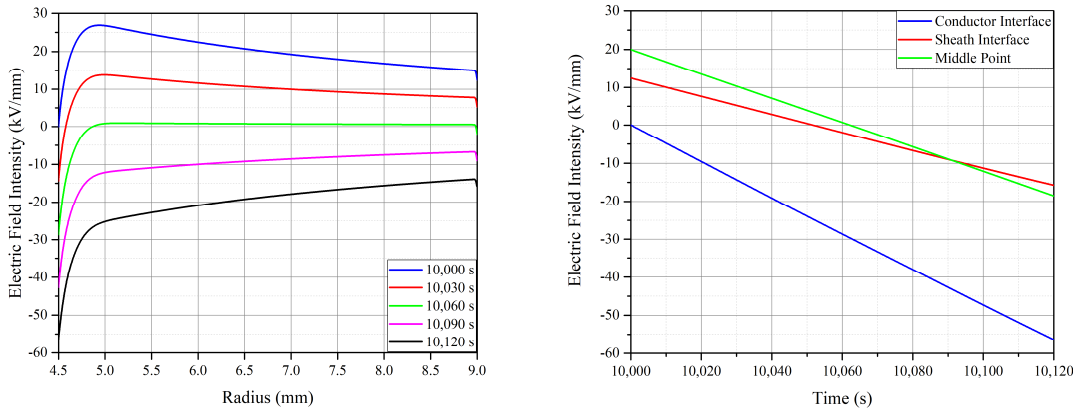


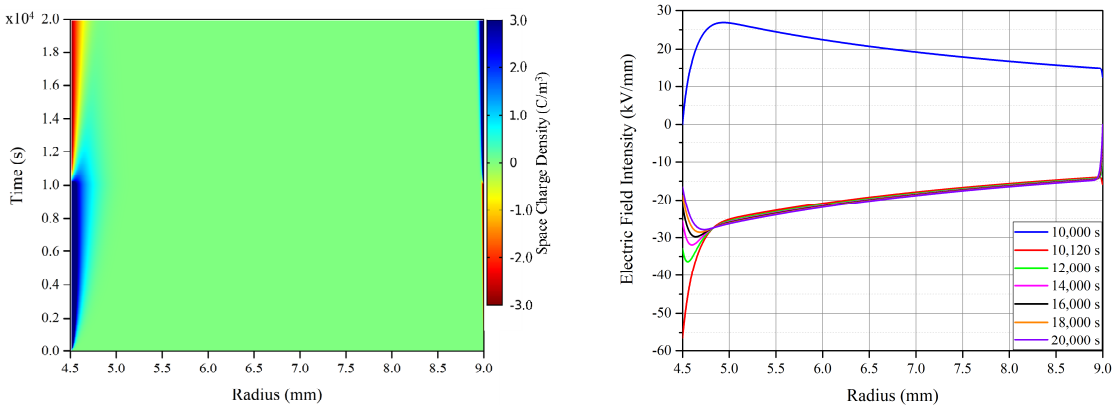

**Figure 7.** Space charge distribution at 250 A: (**a**) Conductor side charge density (C/m$^3$); (**b**) sheath side charge density (C/m$^3$).

Figure 9 shows the space charge distribution and the field distribution after the polarity reversal was completed. Due to the high temperature at the conductor side, a relatively deeper range of charge distribution than the sheath side changed, as shown in Figure 9a. In addition, charges were accumulated at both interfaces over time, but no charge was accumulated at all in the central bulk portion of the insulation regardless of the polarity change.




(**a**) (**b**)

**Figure 8.** Time-varying electric field distribution at 250 A: (**a**) Within low-density polyethylene (LDPE); (**b**) at each point.




(**a**) (**b**)

**Figure 9.** Simulation results after polarity reversal at 250 A: (**a**) Space charge density within LDPE ($C/m^3$); (**b**) time-varying electric field distribution.

Such a charge behavior made the change in electric field intensity at both interfaces prominent. In Figure 9b, the electric field strength at both interfaces gradually decreased and eventually formed a field distribution similar to the shape in which only direction of the field was reversed before the polarity reversal occurred.

Figure 10 shows the time-varying space charge distribution on the both electrode sides at 350 A. Due to the high temperature compared to the case of 250 A, the space charge distribution in the vicinity of the conductor rapidly changed according to the voltage polarity. As a result, at 10,120 s when polarity reversal was completed, the distribution at the conductor side was homo-charged, as shown in Figure 10a.

Figure 11 represents the time-varying electric field distribution. As shown in Figure 11a, it was found that the electric field intensity at conductor interface was reduced due to the influence of the homo-charge distribution. In addition, the location of maximum electric field was inside the LDPE where the polarity of space charge was changed. As a result, the maximum electric field intensity was 47.62 kV/mm at a radius of 4.61 mm, and the active space charge behavior at the high load current contributed to alleviate the electric field concentration immediately after the polarity reversal by homo-charge distribution.

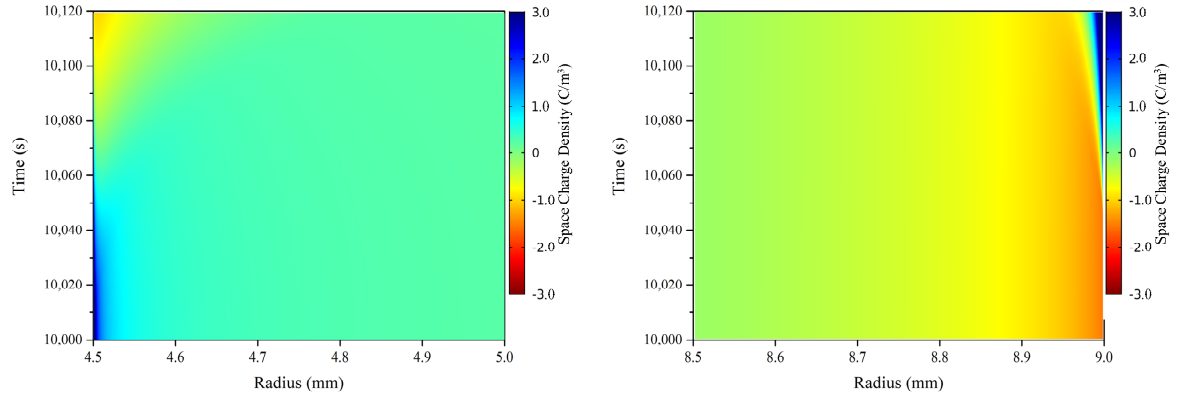



**Figure 10.** Space charge distribution at 350 A: (**a**) Conductor side charge density (C/m$^3$); (**b**) sheath side charge density (C/m$^3$).

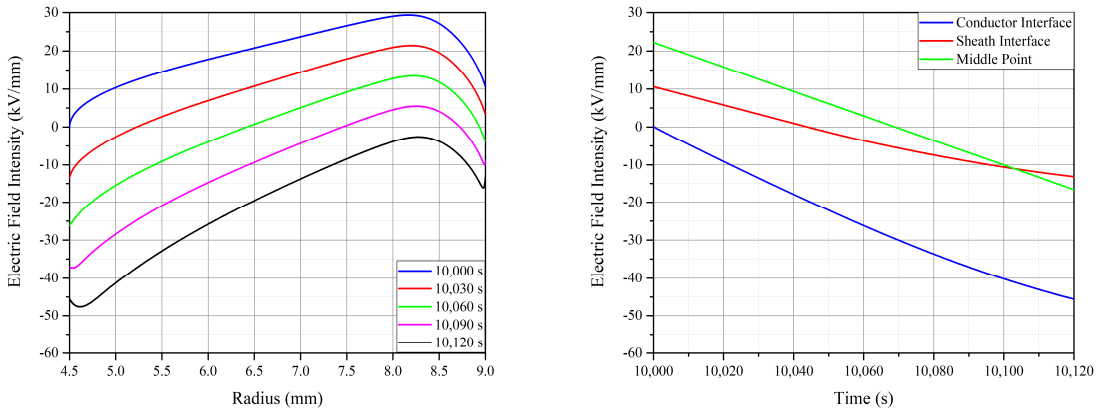



**Figure 11.** Time-varying electric field distribution at 350 A: (**a**) Within LDPE; (**b**) at each point.

The simulation results after polarity reversal in the case of 350 A are shown in Figure 12. It can be seen that the charge penetrated deeply into the bulk due to the increased mobility caused by high temperature as shown in Figure 12a. In addition, Figure 12b shows that a symmetrical electric field distribution was formed with respect to the field distribution before the polarity reversal.

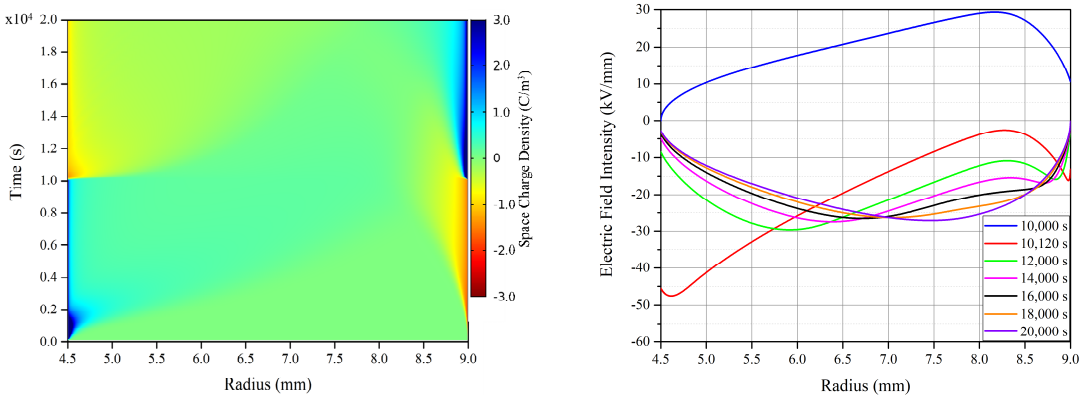



**Figure 12.** Simulation results after polarity reversal at 350 A: (**a**) Space charge density within LDPE (C/m$^3$); (**b**) time-varying electric field distribution.

### *4.2. Polarity Reversal with Electric Potential Zero Duration*

Figures 13 and 14 show the space charge behavior under 250 A at both electrode sides for each electric potential zero duration. In the case of duration 60 s, the change in charge distribution during polarity reversal was insignificant. There was no change in density of the holes at the conductor. As shown in Figure 14a, for the simulation result at duration 1800 s, the density of holes at the conductor interface decreased as it is slowly extracted over the entire time.

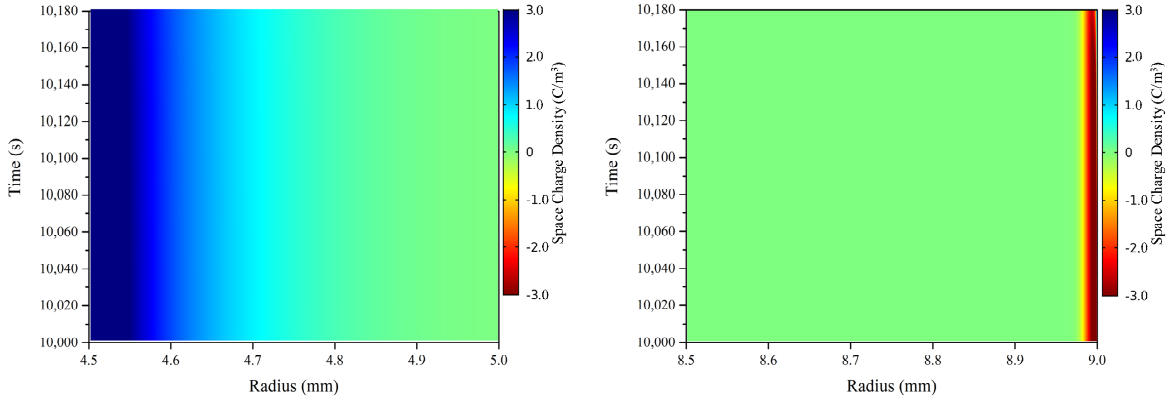



**Figure 13.** Space charge distribution at 250 A and potential zero duration 60 s: (**a**) Conductor side charge density (C/m$^3$); (**b**) sheath side charge density (C/m$^3$).

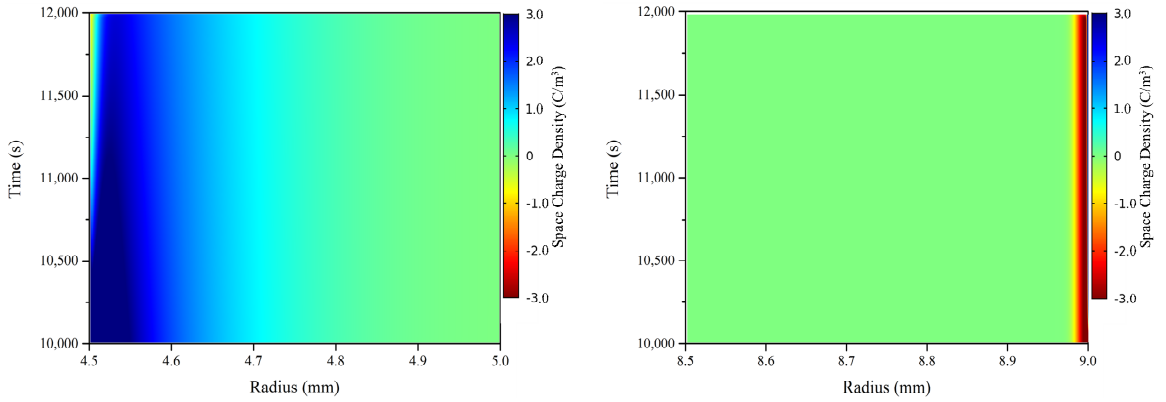
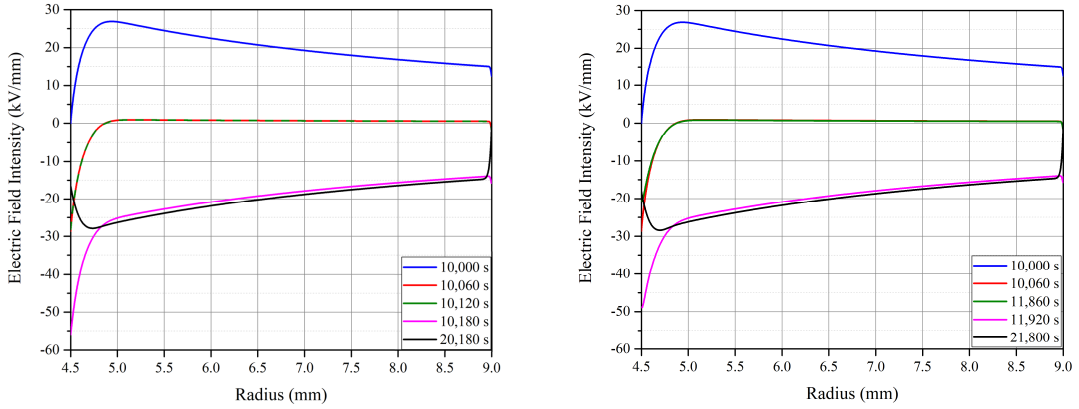



**Figure 14.** Space charge distribution at 250 A and potential zero duration 1800 s: (**a**) Conductor side density (C/m$^3$); (**b**) sheath side density (C/m$^3$).

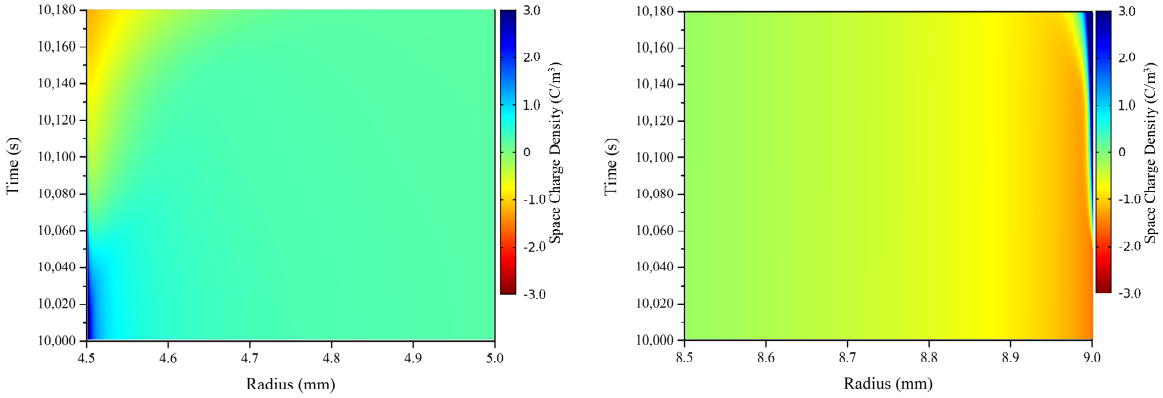
The electric field distributions after polarity reversal in the case of 250 A are shown in Figure 15. During the potential zero duration of 60 s, the electric field intensity at the conductor interface was maintained at a value of 28.61 kV/mm at the conductor interface and increased to 55.93 kV/mm immediately after the polarity reversal. In contrast, for the duration of 1800 s, the field intensity at the conductor interface was gradually decreased from 28.61 kV/mm to 20.53 kV/mm and the maximum electric field strength was 48.83 kV/mm, as shown Figure 15b.




(**a**) (**b**)

**Figure 15.** Time-varying electric field distribution after polarity reversal at 250 A: (**a**) Potential zero duration 60 s; (**b**) 1800 s.

Figure 16 shows the charge behavior under 350 A at both electrode sides for an electric potential zero duration of 60 s. Compared to the result of 250 A, active charge behavior was observed. The density of holes at the conductor side decreased and electrons gradually accumulated. The sheath side began to accumulate holes after 10,050 s. These results were derived by the active injection of holes despite the lower electric field at the sheath side because of the relatively high temperature and low Schottky injection barrier height of holes.




(**a**) (**b**)

**Figure 16.** Space charge distribution at 350 A and potential zero duration 60 s: (**a**) Conductor side charge density (C/m$^3$); (**b**) sheath side charge density (C/m$^3$).

As shown Figure 17a, the long duration time and high temperature allowed the mobile electrons injected from the conductor to transport toward the opposite electrode. However, the holes at the sheath side accumulated locally due to the relatively low mobility on the cable outside, as shown in Figure 17b.

Figure 18 shows the time-varying electric field distribution at 350 A for two potential zero duration times. It was found that the high temperature and long duration significantly reduced the maximum electric field intensity at the conductor side. During the electric potential zero duration of 60 s, the electric field intensity at the conductor interface decreased from 26.16 kV/mm to 22.24 kV/mm, and the maximum field intensity immediately after polarity reversal was 46.82 kV/mm at a radius of 4.63 mm, as shown in Figure 18a.

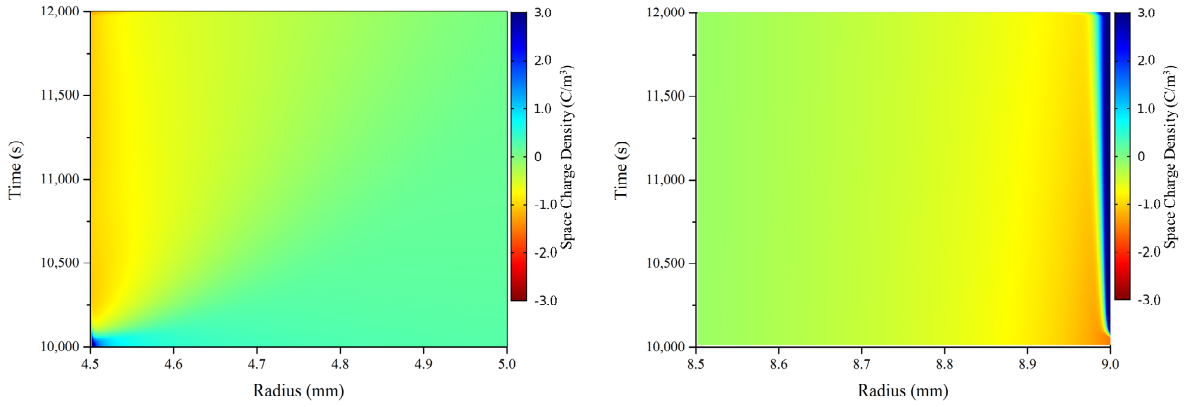



**Figure 17.** Space charge distribution at 350 A and potential zero duration 1800 s: (**a**) Conductor side density (C/m$^3$); (**b**) sheath side density (C/m$^3$).

In case of duration 1800 s, the electric field intensity at the conductor interface was significantly reduced from 26.16 kV/mm to 3.79 kV/mm, and the maximum field intensity immediately after polarity reversal was 38.15 kV/mm at a radius of 4.91 mm. The results for each condition are summarized in Table 3. As a result, the maintenance of the long potential zero duration and high load currents formed a homo-charge at the conductor within the time of polarity reversal, resulting in a decrease in the maximum electric field intensity.

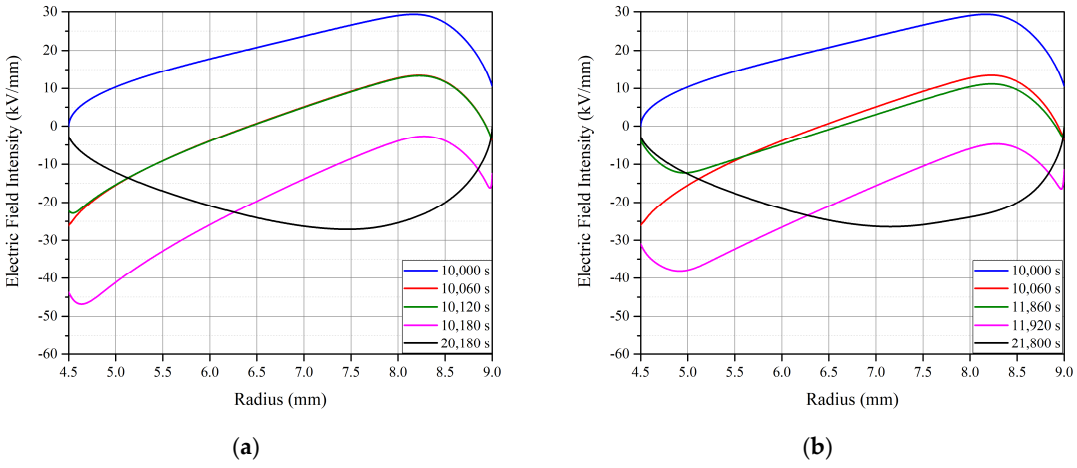



**Figure 18.** Time-varying electric field distribution after polarity reversal at 350 A: (**a**) Potential zero duration 60 s; (**b**) 1800 s.

**Table 3.** Intensity and location of maximum electric field under simulation conditions.

| Potential Zero Duration (s) | Applied Current | | | |
|---|---|---|---|---|
| | 250 A | | 350 A | |
| | $E_{max}$ (kV/mm) | Radius (mm) | $E_{max}$ (kV/mm) | Radius (mm) |
| 0 | 56.34 | 4.5 | 47.62 | 4.61 |
| 60 | 55.93 | 4.5 | 46.82 | 4.63 |
| 1800 | 48.83 | 4.5 | 38.15 | 4.91 |

## 5. Conclusions

We performed a simulation study on the space charge behavior and transient electric field under polarity reversal by applying the BCT model to the cable geometry. The following conclusions can be drawn from this study:

- The modified model is suggested to analyze space charge behavior at transient states such as polarity reversal by modifying boundary conditions.
- The capacitive field was dominant on the electric field distribution during polarity reversal at the low load currents.
- Due to slow space charge behavior at low currents, electric field at the conductor interface was intensified immediately after the polarity reversal at the low load currents.
- The active space charge behavior caused by the high load currents has the effect of alleviating the electric field concentration by forming the homo-charge near the conductor.
- The longer electric potential zero duration contributed to form a homo-charge at the conductor.
- As a result, high load currents and long electric potential zero duration reduced the maximum field strength by 32.3% compared to low load currents without electric potential zero.
- In conclusion, the polarity reversal needs to be performed at the relatively high load currents and sufficiently long electric potential zero duration.

Such numerical approach allowed us to derive the electric field and space charge distribution of insulation under various transients, taking into account the actual operating conditions of HVDC cable systems. In addition, this simulation model can be used for various cable insulation designs in the future by optimizing the parameters of polymeric dielectric such as cross-linked polyethylene (XLPE) or polypropylene (PP).

**Author Contributions:** Conceptualization, S.-J.K.; investigation, S.-J.K.; software, S.-J.K.; writing—original draft preparation, S.-J.K.; supervision, B.-W.L.; writing—review and editing, B.-W.L. All authors have read and agreed to the published version of the manuscript.

**Funding:** This research received no external funding.

**Acknowledgments:** This work was supported by the Korea Institute of Energy Technology Evaluation and Planning(KETEP) and the Ministry of Trade, Industry & Energy(MOTIE) of the Republic of Korea (No. 20174030201780) and by the Korea Electric Power Corporation, Republic of Korea (Grant Number: R17XA05-3).

**Conflicts of Interest:** The authors declare no conflict of interest.

## References

1. Bahrman, M.P.; Johnson, B.K. The ABCs of HVDC transmission technologies. *IEEE Power Energy Mag.* **2007**, *5*, 32–44. [CrossRef]
2. Jeroense, M. HVDC, the next generation of transmission: Highlights with focus on extruded cable systems. *IEEJ Trans. Electr. Electron. Eng.* **2010**, *5*, 400–404. [CrossRef]
3. Murata, Y.; Sakamaki, M.; Abe, K.; Inoue, Y.; Mashio, S.; Kashiyama, S.; Matsunaga, O.; Igi, T.; Watanabe, M.; Asai, S. Development of high voltage DC-XLPE cable system. *SEI Technol. Rev.* **2013**, *101*, 55–62.
4. Hanley, T.L.; Burford, R.P.; Fleming, R.J.; Barber, K.W. A general review of polymeric insulation for use in HVDC cables. *IEEE Electr. Insul. Mag.* **2003**, *19*, 13–24. [CrossRef]
5. Morshuis, P.H.; Bodega, R.; Fabiani, D.; Montanari, G.C.; Dissado, L.A.; Smit, J.J. Calculation and measurement of space charge in MV-size extruded cables systems under load conditions. In Proceedings of the 2007 IEEE International Conference on Solid Dielectrics, Winchester, UK, 8–13 July 2007; pp. 502–505.
6. Le Roy, S.; Teyssedre, G.; Laurent, C.; Montanari, G.C.; Palmieri, F. Description of charge transport in polyethylene using a fluid model with a constant mobility: Fitting model and experiments. *J. Phys. D Appl. Phys.* **2006**, *39*, 1427. [CrossRef]
7. Hoang, A.T.; Serdyuk, Y.V.; Gubanski, S.M. Charge transport in LDPE nanocomposites part II—Computational approach. *Polymers* **2016**, *8*, 103. [CrossRef] [PubMed]

8. Le Roy, S.; Teyssedre, G.; Laurent, C.; Insulation, E. Modelling space charge in a cable geometry. *IEEE Trans. Dielectr. Electr. Insul.* **2016**, *23*, 2361–2367. [CrossRef]
9. Zhan, Y.; Chen, G.; Hao, M. Space charge modelling in HVDC extruded cable insulation. *IEEE Trans. Dielectr. Electr. Insul.* **2019**, *26*, 43–50. [CrossRef]
10. Zhan, Y.; Chen, G.; Hao, M.; Pu, L.; Zhao, X.; Sun, H.; Wang, S.; Guo, A.; Liu, J. Comparison of two models on simulating electric field in HVDC cable insulation. *IEEE Trans. Dielectr. Electr. Insul.* **2019**, *26*, 1107–1115. [CrossRef]
11. Kreuger, F.H. *Industrial High DC Voltage: 1. Fields, 2. Breakdowns, 3. Tests*; Delft University Press: Delft, The Netherlands, 1995.
12. Mazzanti, G.; Marzinotto, M. *Extruded Cables for High-Voltage Direct-Current Transmission: Advances in Research and Development*; John Wiley & Sons: Hoboken, NJ, USA, 2013; Volume 93.
13. Teyssedre, G.; Laurent, C. Charge transport modeling in insulating polymers: From molecular to macroscopic scale. *IEEE Trans. Dielectr. Electr. Insul.* **2005**, *12*, 857–875. [CrossRef]
14. Montanari, G.; Mazzanti, G.; Palmieri, F.; Motori, A.; Perego, G.; Serra, S. Space-charge trapping and conduction in LDPE, HDPE and XLPE. *J. Phys. D Appl. Phys.* **2001**, *34*, 2902. [CrossRef]
15. Liu, N.; Zhou, C.; Chen, G.; Zhong, L. Determination of threshold electric field for charge injection in polymeric materials. *Appl. Phys. Lett.* **2015**, *106*, 192901. [CrossRef]
16. Vu, T.; Teyssedre, G.; Vissouvanadin, B.; Le Roy, S.; Laurent, C.; Mammeri, M.; Denizet, I. Field distribution in polymeric MV-HVDC model cable under temperature gradient: Simulation and space charge measurements. *Eur. J. Electr. Eng.* **2014**, *17*, 307–325.
17. Moore, G.F. *Electric Cables Handbook*; Blackwell Science: Hoboken, NJ, USA, 1997.
18. Mardiana, R. Parameters affecting the ampacity of HVDC submarine power cables. In Proceedings of the 2011 2nd International Conference on Electric Power and Energy Conversion Systems (EPECS), Sharjah, UAE, 15–17 November 2011; pp. 1–6.
19. Almallah, M.R. *Ampacity of HV Multi-Insulation Cables at Different Cooling Methods: HVAC and HVDC Power Cables*; Scholars' Press: Saarbrücken, Germany, 2016.
20. Jeroense, M.; Morshuis, P. Electric fields in HVDC paper-insulated cables. *IEEE Trans. Dielectr. Electr. Insul.* **1998**, *5*, 225–236. [CrossRef]
21. Takada, T. Acoustic and optical methods for measuring electric charge distributions in dielectrics. In Proceedings of the 1999 Annual Report Conference on Electrical Insulation and Dielectric Phenomena (Cat. No. 99CH36319), Austin, TX, USA, 17–20 October 1999; pp. 1–14.




© 2020 by the authors. Licensee MDPI, Basel, Switzerland. This article is an open access article distributed under the terms and conditions of the Creative Commons Attribution (CC BY) license (http://creativecommons.org/licenses/by/4.0/).